# TRANSITIONS OF ZONAL FLOWS IN A TWO-LAYER QUASI-GEOSTROPHIC OCEAN MODEL

Henk Dijkstra, Taylan Sengul, Mickael D Chekroun, Shouhong Wang

# TRANSITIONS OF ZONAL FLOWS IN A TWO-LAYER QUASI-GEOSTROPHIC OCEAN MODEL

MICKAEL D. CHEKROUN, HENK DIJKSTRA, TAYLAN ŞENGÜL, AND SHOUHONG WANG

ABSTRACT. We consider a 2-layer quasi-geostrophic ocean model where the upper layer is forced by a steady Kolmogorov wind stress in a periodic channel domain, which allows to mathematically study the nonlinear development of the resulting flow. The model supports a steady parallel shear flow as a response to the wind stress. As the maximal velocity of the shear flow (equivalently the maximal amplitude of the wind forcing) exceeds a critical threshold, the zonal jet destabilizes due to baroclinic instability and we numerically demonstrate that a first transition occurs. We obtain reduced equations of the system using the formalism of dynamic transition theory and establish two scenarios which completely describe this first transition. The generic scenario is that two modes become critical and a Hopf bifurcation occurs as a result. Under an appropriate set of parameters describing midlatitude oceanic flows, we show that this first transition is continuous: a supercritical Hopf bifurcation occurs and a stable time periodic solution bifurcates. We also investigate the case of double Hopf bifurcations which occur when four modes of the linear stability problem simultaneously destabilize the zonal jet. In this case we prove that, in the relevant parameter regime, the flow exhibits a continuous transition accompanied by a bifurcated attractor homeomorphic to $S^3$. The topological structure of this attractor is analyzed in detail and is shown to depend on the system parameters. In particular, this attractor contains (stable or unstable) time-periodic solutions and a quasi-periodic solution.

## CONTENTS



## 1. INTRODUCTION

Baroclinic instability is among the most important geophysical fluid dynamical instabilities playing a crucial role in the dynamics of atmospheres and oceans. In particular, this instability mechanism is the dominant process in atmospheric dynamics shaping the cyclones and anticyclones that dominate weather in mid-latitudes, as well as the mesoscale ocean eddies that play various roles in oceanic dynamics and the transport of heat of salt [26]. Much is known on the linear stability of zonal jets in a horizontally unbounded ocean in the quasi-geostrophic (QG) flow regime. Classical models, such as the continuously stratified Eady model [9] and the two-layer Phillips model [20], have lead to a detailed understanding of the mechanism of baroclinic instability of a zonal jet in

*Date*: October 9, 2021.

the inviscid case. Long waves destabilize the zonal jet with maximum growth rates occurring for perturbations having wavelengths on the order of the Rossby deformation radius, typically $50-100$ km for the mid-latitude ocean [25].

In case linear friction is included in the two-layer model, the neutral curve has a minimum at $(k_c, \mu_c)$ where $k_c$ is the critical wavenumber and $\mu_c$ the critical value of the control parameter (e.g. the maximum speed of the zonal jet). The nonlinear development of these perturbations has been extensively analyzed in the weakly nonlinear case [19, 21, 29, 13]. In the regime $|k-k_c| = \mathcal{O}(\epsilon)$ and $|\mu-\mu_c| = \mathcal{O}(\epsilon^2)$, [27] showed that on a long time scale $T = \epsilon^2 t$ and large spatial scale $X = \epsilon(x - c_g t)$, where $c_g$ is the group velocity of the waves at criticality, the complex amplitude $A$ of the wave packet destabilizing the jet satisfies a Ginzburg-Landau equation, written as

$$\frac{\partial A}{\partial T} = \gamma_1 A + \gamma_2 \frac{\partial^2 A}{\partial X^2} - \gamma_3 A|A|^2,$$

where the $\gamma_i$ are complex constants. [27] also showed that the fixed point solution of this equation can become unstable to sideband instabilities. Subsequent analysis has shown [7] that upgradient momentum transport can occur due to the self-interaction of the instabilities leading to rectification of the zonal jet.

In reality, the ocean basins are zonally bounded by continents and the midlatitude zonal jets are part of the gyre system, for example the subpolar gyre and subtropical gyre in the North Atlantic, forced by the surface wind stress through Ekman pumping [18]. The problem of baroclinic instability of such non-parallel flows is much more complicated and has so far only been tackled numerically. When the wind-forced QG equations are discretized, the linear stability problem for the gyre flow results in a large-dimensional generalized eigenvalue problem, typically of dimension $10^4$. There are many results for the one-layer single- and double-gyre flows (for an overview, see chapter 5 of [5]), but in this case there is no baroclinic instability. There are relatively few results for the two-layer case. In [6], it was shown that in the two-layer case the double-gyre flow becomes unstable through a sequence of Hopf bifurcations. The perturbation flow patterns at criticality are 'banana-shaped', locally resembling those of baroclinic instability in the Philips model. Stable periodic orbits result from these Hopf bifurcations, typically given rise to meandering motion of the gyre boundary.

As an intermediate, more analytically tractable case, we consider here the baroclinic instability of a zonal jet for a two-layer QG model in a zonally periodic channel. In this case, the properties of the bounded geometry are somehow represented, as the patterns of the unstable modes are restricted by the periodicity of the channel, so a sequence of Hopf bifurcations is expected just as in the more realistic gyre case. In addition, parallel flow solutions exist in the zonally periodic channel which simplifies the linear stability problem substantially such that a more detailed nonlinear analysis, akin to that in the horizontally unbounded case, can be performed. The parallel flow can also be connected to the surface wind stress, as in the full gyre case, but at the expense of adding an additional linear friction term to the upper layer vorticity equation; for more details, see Section 2 below.

The case specifically studied in the paper is the circulation set up by a time-independent Kolmogorov wind-stress field (for $k = 1, 2, \ldots$)

$$\tau^x(y) = -\tau \frac{\tau_0}{k\pi} \cos k\pi \frac{y}{L_y} \; ; \; \tau^y = 0$$

where $\tau_0$ is a characteristic mid-latitude wind-stress value. This wind stress forces an ocean enclosed in a rectangular basin $[0, 2L_x] \times [-L_y, L_y]$ on the $\beta$-plane. The case $k = 1$ and $k = 2$ are often referred to as the single- and double-gyre forcing. The stratification is modeled in terms of a two-layer system and the wind stress only directly forces the upper layer. As a response to this wind stress, the system supports a basic shear flow $\psi^s$. The amplitude $\tau$ that controls the wind-stress curl, or equivalently the maximal velocity of the shear flow $\psi^s$ is chosen as the bifurcation parameter.

We first perform a numerical linear stability analysis of this basic shear flow; for small values of $\tau$, all associated eigenvalues have negative real parts such that the jet is stable. When the aspect ratio of the channel $a = L_y/L_x$ is large, the eigenvalues remain in the left complex plane regardless of the value of $\tau$. However, when the aspect ratio gets small, the basic shear flow loses stability at a critical $\tau$ in the form of a pair of single or double complex eigenvalues crossing the imaginary axis, giving rise to a Hopf or double Hopf bifurcation. We next use the idea and method of the dynamic transition theory [15, 16], which is aimed to determine all the local attractors near a transition. The approach comes with a classification of all transitions into three classes

known as continuous, catastrophic and random types. In this way, our study extends previous results using this approach on the single-layer barotropic case [24, 8], the two-layer case for constant zonal jet velocities [2] and the barotropic Munk western boundary layer current profile case [10], to the zonally periodically bounded two-layer case.

Using the center manifold reduction, we obtain reduced (ordinary differential equation, ODE) models describing this transition. From the coefficients of these ODEs, the transition numbers in dynamic transition theory can be calculated. The case of a Hopf bifurcation is generic while the case of a double Hopf bifurcation is degenerate and requires fine tuning of the aspect ratio to critical values where two pairs of eigenmodes with consecutive wavenumbers cross the imaginary axis simultaneously. Under standard set of parameters describing the midlatitude ocean, we perform numerical computations of the transition number for the forcing patterns corresponding to $k = 1, 2, 3$ and the aspect ratios $a \geq 3$. We find that in the parameter regimes we are interested with, the Hopf bifurcation is supercritical and a stable limit cycle bifurcates. For the double Hopf bifurcation, we find that after the corresponding transition takes place, the system exhibits a bifurcated local attractor [15] near the basic shear flow which is homeomorphic to the 3D-sphere. The topological structure of this attractor is analyzed and depending on the parameters, it is found to contain a combination of limit cycles and a quasi periodic solution.

The paper is organized as follows. In section 2, the quasi-geostrophic model is presented. This is followed by section 3 where the theory and numerical results for the linear stability problem (section 3.1), the Hopf bifurcation case (section 3.2) and the double-Hopf bifurcation case (section 3.3) are presented. These results are summarized and discussed in section 4. The appendix contains details on the proofs of the theorems and on the numerical computations.

## 2. The model

We consider two layers of homogeneous fluids, each with a different and constant density $\rho_1$ and $\rho_2$ and with equilibrium layer thicknesses $H_1$ and $H_2$, on a mid-latitude $\beta$-plane with Coriolis parameter is $f = f_0 + \beta_0 y$. The lighter fluid in layer 1 is assumed to lie on top of the heavier one in layer 2 so that the stratification is statically stable, i.e., $\rho_1 < \rho_2$; bottom topography is neglected.

This flow can be modeled by the two-layer QG model [19] using the geostrophic stream function $\psi_i$ and the vertical component of the relative vorticity $\zeta_i$ in each layer ($i = 1, 2$). The quantities $\psi_i$ and $\zeta_i$ are non-dimensionalised by $UL_y$ and $U/L_y$, respectively, wind stress with $\tau_0$, length with $L_y$, and time with $L_y/U$, where $U$ is a characteristic horizontal velocity. By choosing $U = \tau_0/(\rho_0\beta_0 L_y H_1)$, where $\rho_0$ is a reference density, the dimensionless equations on the domain $(0, 2/a) \times (-1, 1)$ become

$$\begin{aligned} \left[\frac{\partial}{\partial t} + \{\psi_1, \cdot\}\right](\Delta\psi_1 + F_1(\psi_2 - \psi_1) + \beta y) &= \mathcal{F}_1 - \tau\beta \sin k\pi y \\ \left[\frac{\partial}{\partial t} + \{\psi_2, \cdot\}\right](\Delta\psi_2 + F_2(\psi_1 - \psi_2) + \beta y) &= -r_2\Delta\psi_2 \end{aligned} \tag{2.1}$$

where $\{f, g\} = f_x g_y - f_y g_x$ is the usual Jacobian operator and $\mathcal{F}_1$ represents the damping of upper layer vorticity due to frictional processes (to be specified below). In the bottom layer, we include a linear (Ekman) friction term $-r_2\Delta\psi_2$; in both layers, Laplacian friction terms are neglected due to the absence of continental boundary layers making such terms much smaller than the other ones. The expressions for the dimensional and dimensionless parameters, with their standard values at a latitude 45°N, are given in Table 1.

For the boundary conditions, we assume periodicity in the $x$-direction and free-slip boundaries in the $y$-direction. Hence, the conditions are

$$\begin{aligned} &\psi_i\,|_{x=0} = \psi_i\,|_{x=2/a}, \qquad i = 1, 2. \\ &\psi_i\,|_{y=\pm1} = \frac{\partial^2\psi_i}{\partial y^2}\,|_{y=\pm1} = 0, \qquad i = 1, 2. \end{aligned} \tag{2.2}$$

In actual ocean basins, a steady zonal jet is generated by the applied wind stress through Ekman pumping, a Sverdrup balance and a western boundary layer flow [18]. Due to the periodic boundary conditions used here,

such a flow cannot be captured in this model. However, the equations will allow a steady state of the form

$$\psi_1^s = \Psi \sin k\pi y, \qquad \psi_2^s = 0 \tag{2.3}$$

which relates to the wind stress field, when $\mathcal{F}_1 - \tau\beta \sin k\pi y = 0$. In this paper, we will assume that the wind-stress vorticity input is balanced by vorticity decay due to the linear friction term $\mathcal{F}_1 = -r_1\Delta\psi_1$, being aware that a larger friction coefficient $r_1$ is needed than can be justified from existing dissipative processes in the ocean. In this case, it follows that

$$\Psi = \frac{\tau\beta}{(k\pi)^2 r_1}. \tag{2.4}$$

The parameter $\Psi$ appearing in (2.3) can then be chosen as the control parameter as is the case in this study, instead of $\tau$.

By considering the perturbation $\psi_i' = \psi_i - \psi_i^s$, $i = 1, 2$, we can write the system in the following operator form.

$$\mathcal{M}\partial_t\psi = \mathcal{N}\psi + \mathcal{G}(\psi), \qquad \psi = (\psi_1, \psi_2) \tag{2.5}$$

where $\mathcal{M}$ and $\mathcal{N}$ are the linear operators defined as

$$\mathcal{M}\psi = \begin{bmatrix} \Delta\psi_1 + F_1(\psi_2 - \psi_1) \\ \Delta\psi_2 + F_2(\psi_1 - \psi_2) \end{bmatrix} \tag{2.6}$$

$$\mathcal{N}\psi = \begin{bmatrix} \Psi k\pi \cos k\pi y \left( (k\pi)^2 \frac{\partial\psi_1}{\partial x} + F_1 \frac{\partial\psi_2}{\partial x} + \frac{\partial\Delta\psi_1}{\partial x} \right) - \beta\frac{\partial\psi_1}{\partial x} - r_1\Delta\psi_1 \\ -\Psi k\pi F_2 \frac{\partial\psi_2}{\partial x} - \beta\frac{\partial\psi_2}{\partial x} - r_2\Delta\psi_2 \end{bmatrix} \tag{2.7}$$

Lastly, the bilinear nonlinearity is given explicitly by

$$\mathcal{G}(\psi) = \begin{bmatrix} -\{\psi_1, \Delta\psi_1 + F_1(\psi_2 - \psi_1)\} \\ -\{\psi_2, \Delta\psi_2 + F_2(\psi_1 - \psi_2)\} \end{bmatrix} \tag{2.8}$$

In terms of function spaces, the operators $\mathcal{G}$ and $\mathcal{N}$ are the mappings, $\mathcal{G} : H_1 \to H_{-1}$ and $\mathcal{N} : H_0 \to H_{-1}$, where

$$\begin{aligned} H_1 &= \{\psi = (\psi_1, \psi_2) \in H^4(\Omega) \times H^4(\Omega) |\ \psi \text{ satisfies (2.2)}\}, \\ H_0 &= \{\psi = (\psi_1, \psi_2) \in H^2(\Omega) \times H^2(\Omega) |\ \psi \text{ satisfies (2.2)}\}, \\ H_{-1} &= L^2(\Omega)^2. \end{aligned}$$

Here $\Omega = (0, 2/a) \times (-1, 1)$ and $H^4(\Omega)$, $H^2(\Omega)$, $L^2(\Omega)$ are the usual Sobolev and Lebesgue function spaces endowed with their natural inner products. These space account for spatial regularity of the solution $\psi$ for which $H^p(\Omega)$ denotes the space of square-integrable functions that possess $p$th-order derivatives (in the distribution sense) that are themselves square-integrable; see e.g. [1].

## 3. Results

In this section, we first present the linear stability analysis of the basic shear flow and then we move on to describe the first transitions due to the instabilities, covering both the Hopf and double Hopf bifurcations.

### 3.1. Linear Stability Analysis.

We first investigate the linear stability of the basic solution. For this purpose, we denote the eigenmodes of the linear problem by

$$\psi_{m,j}(x, y) = e^{i\alpha_m x} Y_j(y), \qquad j \in \mathbb{N}, m \in \mathbb{Z}, \quad \alpha_m := am\pi.$$

with eigenvalues $\sigma_{m,j}$, i.e.

$$\sigma_{m,j}\mathcal{M}\psi_{m,j} = \mathcal{N}\psi_{m,j}. \tag{3.1}$$

Since the linear operators $\mathcal{M}$ and $\mathcal{N}$ are real, we have

$$\overline{\sigma_{m,j}} = \sigma_{-m,j}, \qquad \overline{\psi_{m,j}} = \psi_{-m,j}, \qquad \forall m \in \mathbb{N}.$$

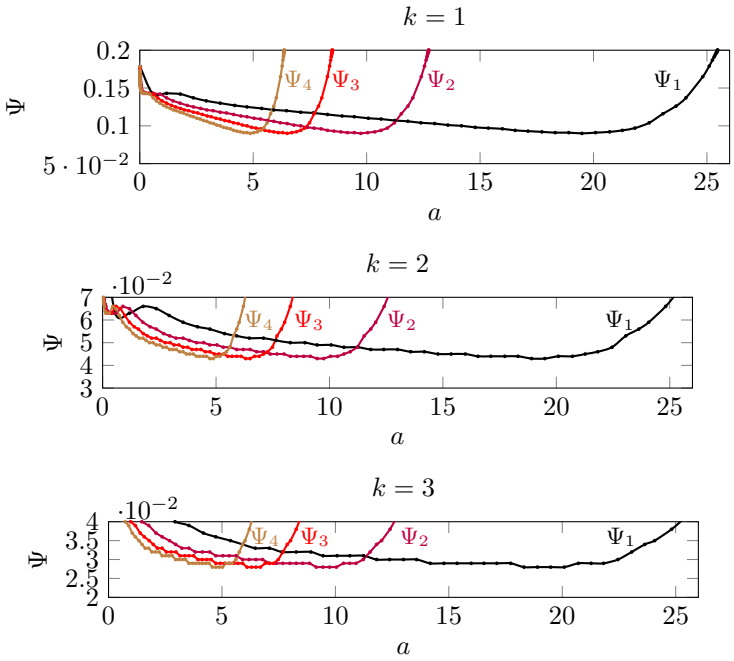


FIGURE 1. Neutral stability curves $\Psi_m, m = 1, 2, 3, 4$ defined in (3.2), for wind-stress profiles defined by $k = 1, 2, 3$. For values of $\Psi > \Psi_m$, the shear flow $\Psi^s$ becomes unstable to a perturbation pattern with wavenumber $\alpha_m$.

This eigenvalue problem is solved numerically by means of a standard Legendre-Galerkin method; see Appendix A. A typical picture of the spectrum near the criticality is given in Figure 3. This figure shows that many eigenvalues are clustered near the imaginary axis at the critical value of $\Psi_c$ as defined below.

We assume (as will be confirmed by the numerical results) that the eigenvalues are ordered so that for each $m \in \mathbb{Z}$, $\sigma_{m,1}$ has the largest real part among $\sigma_{m,j}$, $j \in \mathbb{N}$.

For each $m \in \mathbb{N}$, we define $\Psi_m$, if it exists, to be the value of $\Psi$ for which the eigenvalue $\sigma_{m,1}$ crosses the imaginary axis, that is

$$Re(\sigma_{m,1}) = Re(\sigma_{-m,1}) = \begin{cases} < 0, & \text{if } \Psi < \Psi_m \\ = 0, & \text{if } \Psi = \Psi_m \\ > 0, & \text{if } \Psi > \Psi_m \end{cases} \tag{3.2}$$

Hence $\Psi = \Psi_m$ defines a neutral stability curve in the $a - \Psi$ plane. In Figure 1, these neutral curves are plotted for zonal wave numbers $m = 1, 2, 3, 4$.

Our numerical analysis suggests that for $m$ in $\mathbb{N}$, $\Psi_m$ exists only for aspect ratios of the basin characteristic lengths smaller than a threshold $a_m$, that is for $a < a_m$. The threshold $a_m$ is defined by the vertical asymptote condition,

$$\lim_{a \to a_m -} \Psi_m = \infty.$$

Moreover,

$$\infty > a_1 > a_2 > \cdots$$

We define the **critical maximal amplitude** $\Psi_c$ of the steady state given in (2.3) and the critical zonal wavenumber $m_c$ by

$$\Psi_c = \min_{m \in \mathbb{N}} \Psi_m.$$

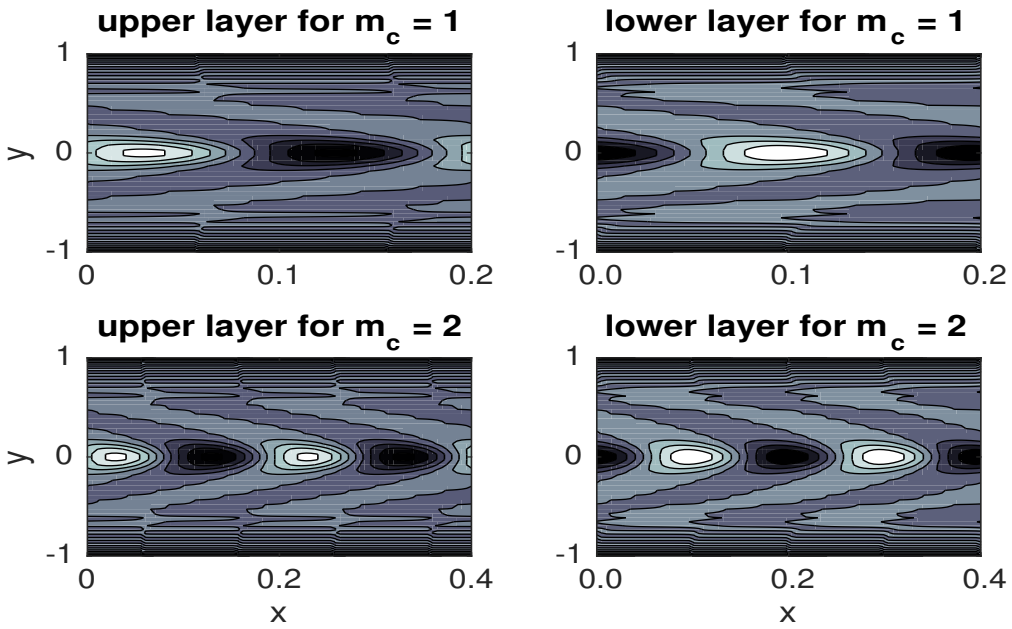


FIGURE 2. Real part of the upper and lower layers of the time-periodic solution $f_{m_c}$ (or equivalently of the dominant eigenmode $\psi_{m_c,1}$) at $t = 0$ for $k = 1$ and $a = 10$ and $a = 5$, respectively.

$$m_c = \underset{m\in\mathbb{N}}{\operatorname{argmin}} \Psi_m.$$

The typical structure of the spectrum at the critical parameter $\Psi = \Psi_c$ is shown in Figure 3 where a pair of complex conjugate eigenvalues cross the imaginary axis. The eigenvalues on the real axis belong to wavenumber $m = 0$ and are always stable although in Figure 3 it looks like as if there is an additional critical real eigenvalue.

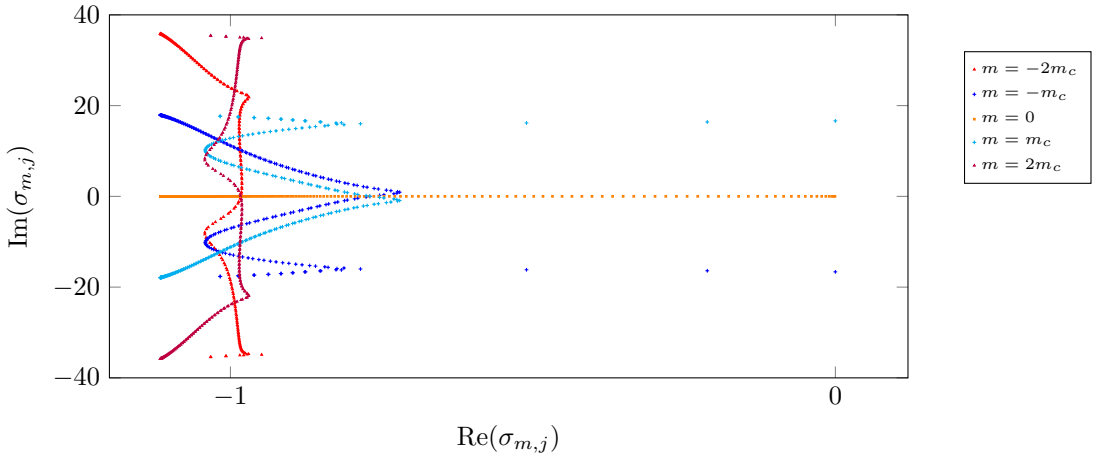


FIGURE 3. The first 240 eigenvalues at the critical parameter when $m_c = 2$, $a = 10$, $k = 1$ and $N_y = 240$.

To describe the solutions near the onset of transition $\Psi = \Psi_c$, we define the spatio-temporal function

$$f_m(x, y, t) = 2\,\mathrm{Re}\left(e^{i\,\mathrm{Im}(\sigma_{m,1})t}\psi_{m,1}(x, y)\right), \quad m \in \mathbb{Z}, \tag{3.3}$$

where $\sigma_{m,1}$ is the first eigenvalue and $\psi_{m,1}$ is its associated eigenfunction. The spatial structure of the eigenmodes $\psi_{m_c,1}$ is shown in Figure 2, revealing the well-known 'banana-shaped' patterns characteristics of baroclinic instability.

The values of $\Psi_c$ with respect to the aspect ratio $a$ for $k = 1, 2, 3$ is shown in Figure 5. By the previous remarks,

$$\lim_{a\to a_1-} \Psi_c = \lim_{a\to a_1-} \Psi_1 = \infty. \tag{3.4}$$

By (3.4), *for $a > a_1$, the system is linearly stable.* As is expected, the neutral stability curves (Figure 1) approach the asymptote $\Psi_c \to \infty$ as $a$ increases to the critical aspect ratio $a_1$ over which the system is linearly stable for all $\Psi$. The value of $\Psi_c \approx 0.09/k$ for small $a$ for each $k = 1, 2, 3$, see Figure 5. This value of critical maximal shear velocity corresponds to an upper layer friction, (2.4) which is approximately,

$$r_1 \approx \frac{\tau\beta}{k^2\pi^2\Psi_c} \approx \frac{1000.0}{k},$$

which is indeed much larger than can be justified from dissipative processes in the ocean but, as explained in section 2, is needed here to connect the zonal jet top the wind-stress field.

The friction term in the lower layer however is physical (Ekman friction) and for this study, it is fixed at $r_2 = 5.0$, see Table 1. Also, from Figure 1, we see that for small aspect ratios, many modes become unstable as $\Psi_c$ is exceeded.

For $a < a_1$, the system has a first transition at $\Psi = \Psi_c$ and exactly one of the following two principal of exchange of stability (PES) condition holds:

$$\begin{aligned} Re(\sigma_{m,1}) = Re(\sigma_{-m,1}) &\begin{cases} < 0, \text{ if } \Psi < \Psi_c \\ = 0, \text{ if } \Psi = \Psi_c \\ > 0, \text{ if } \Psi > \Psi_c \end{cases} && \text{if } m = m_c \\ Re(\sigma_{m,1}) = Re(\sigma_{-m,1}) < 0 & && \text{if } m \neq m_c \end{aligned} \tag{3.5}$$

$$\begin{aligned} Re(\sigma_{m,1}) = Re(\sigma_{-m,1}) &\begin{cases} < 0, \text{ if } \Psi < \Psi_c \\ = 0, \text{ if } \Psi = \Psi_c \\ > 0, \text{ if } \Psi > \Psi_c \end{cases} && \text{if } m \in \{m_c, m_c+1\} \\ Re(\sigma_{m,1}) = Re(\sigma_{-m,1}) < 0 & && \text{if } m \notin \{m_c, m_c+1\}. \end{aligned} \tag{3.6}$$

According to (3.5) and (3.6) either, two or four eigenvalues become unstable as $\Psi$ crosses $\Psi_c$. The case of two critical eigenvalues is generic and results in a Hopf bifurcation. The case of four critical eigenvalues results in a double Hopf bifurcation and requires the fine-tuning of the aspect ratio $a = a_{DH}$ so that $\Psi_c = \Psi_{m_c} = \Psi_{m_c+1}$. The values of $a_{DH}$ where double Hopf transition occurs is given in Table 2. Although the double Hopf transition is not generic, its analysis gives an insight into the moderate $\Psi$ regime where multiple eigenvalues are unstable. In Figure 4, we present the dominant part of the spectrum of the linearized operator at a critical aspect ratio $a_{DH}$.

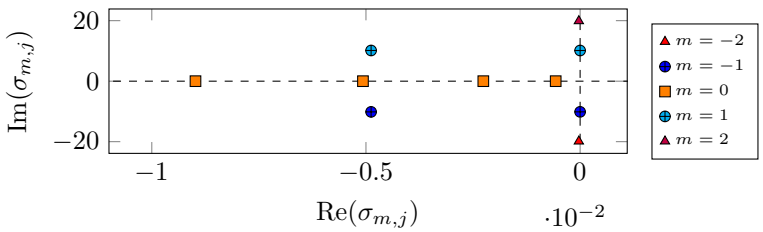


FIGURE 4. The spectrum near the double Hopf aspect ratio $a_{DH} = 11.263$ for $k = 1$. The first four critical eigenvalues $\sigma_{m,1}$, $m \in \{-2, -1, 1, 2\}$, can be seen on the imaginary axis.

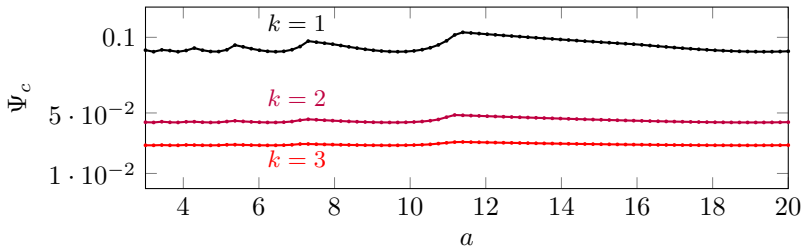


FIGURE 5. The critical maximal shear steady state velocity $\Psi_c$ with respect to channel aspect ratio $a$ for $k=1,2,3$ where the PES condition (3.5) holds.

Our numerical results in Figure 1 and Figure 5 verify the PES condition for the chosen parameter values. The PES condition (3.5) has been rigorously verified for Kolmogorov flows in [17] via a continued fraction method. This method has later been extended for the single layer QG model for the $k=1$ case in [24] and for $k\geq 2$ in [14] where $k$ is the forcing frequency in (2.1). It is still an open problem to prove this claim for the current problem.

3.2. **Hopf Bifurcation.** We first investigate the generic Hopf transition scenario based on the attractor bifurcation theorem [15, Theorem 5.2] and the dynamical transition theorem [16, Theorem 2.1.3]. For proofs of the following lemma and theorem, see Appendix B).

**Lemma 3.1.** *Assume that the first critical eigenvalue is complex simple so that the PES condition (3.5) holds. Then the transition and stability of the steady state solution (2.3) of the equation (2.5) in the vicinity of the critical maximal shear velocity $\Psi=\Psi_c$ and for any sufficiently small initial condition are equivalent to the stability of the zero solution of the equation*

$$\frac{dz}{dt}=\sigma_{m_c,1}z+Pz|z|^2+o(|z|^3). \tag{3.7}$$

*where $z(t)$ which lies in $\mathbb{C}$ denotes the amplitude of the projection of the solution onto the first eigenfunction $\psi_{m_c,1}$ and the complex number $P$ denotes the **transition number** defined in Eq. (B.8) of Appendix B.*

The analysis of Lemma 3.1 yields the following theorem.

**Theorem 3.1.** *Assume that the first critical eigenvalue has simple complex multiplicity, that is the PES condition (3.5) is satisfied. Then the following assertions hold true.*

*(1) If $\mathrm{Re}(P)<0$, the system (2.5) undergoes a continuous transition accompanied by a supercritical Hopf bifurcation on $\Psi>\Psi_c$. In particular, the steady-state solution bifurcates to a stable periodic solution $\psi$ on $\Psi>\Psi_c$, satisfying $\psi\to\mathbf{0}$ as $\Psi\to\Psi_c$ and has the following approximation*

$$\psi(x,y,t)=\left(\frac{-\mathrm{Re}(\sigma_{m_c,1})}{\mathrm{Re}(P)}\right)^{\frac{1}{2}}f_{m_c}(x,y,t)+o\left(|\Psi-\Psi_c|^{\frac{1}{2}}\right). \tag{3.8}$$

*The spatial structure of the time periodic solution $\psi$ is shown at $t=0$ for different aspect ratios $a$ in Figure 2.*

*(2) If $\mathrm{Re}(P)>0$, the system (2.5) undergoes a jump transition on $\Psi<\Psi_c$ accompanied by a subcritical Hopf bifurcation. In particular, an unstable periodic orbit $\psi$ given by (3.8) bifurcates on $\Psi<\Psi_c$ and there is no periodic solution bifurcating from $\mathbf{0}$ on $\Psi>\Psi_c$. Moreover, there is a singularity separation at some $\Psi_s<\Psi_c$ generating an attractor and an unstable periodic orbit $\psi$.*

When the PES condition (3.5) holds, the system exhibits a Hopf bifurcation as described by Theorem 3.1. The type of transition boils down to the determination of the transition number $P$ given in (B.8) of Appendix B. For the practical calculation of this number, we refer to Appendix C. Our analysis given in Figure 6 shows that for low forcing frequencies $k=1,2,3$, *generally* $Re(P)<0$ and as a result *only continuous transition (supercritical Hopf bifurcation) is possible for the parameter regime we have selected.* In Figure 6, we also display the critical wavenumber $m_c$. In the range $4\leq a\leq 20$, the critical wavenumber is found to $1\leq m_c\leq 4$.

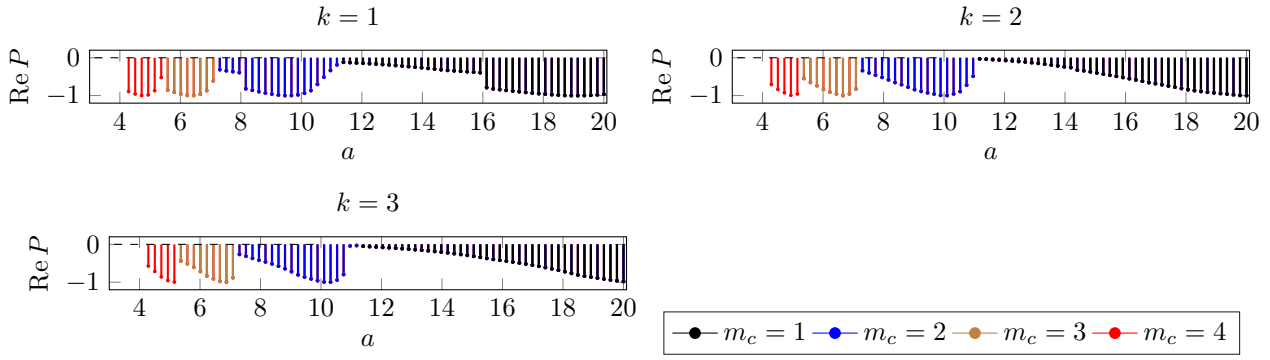


FIGURE 6. The real part of the transition number $P$ compared to the channel aspect ratio $a$ normalized by the largest absolute value of $\operatorname{Re} P$. The parameters are as set in Table 1.

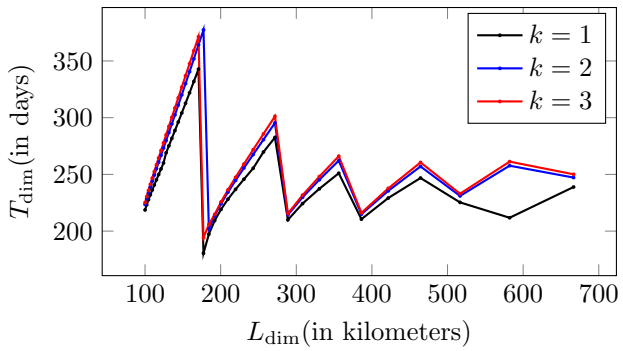


FIGURE 7. The (dimensional) time period $T_{\text{dim}} = \frac{2\pi}{\operatorname{Im}(\sigma_{m_c,1})}\frac{L_y}{U}$ compared to the (dimensional) length of the channel $L_{\text{dim}} = 2L_y/a$ of the both stable and unstable bifurcated time periodic solution (3.8) in the Hopf bifurcation case. Here $L_y$ and $U$ are the characteristic scales defined in Table 1. The jumps in the derivative of the time period of the bifurcated solution is due to the change of the imaginary part $\operatorname{Im}\sigma_{m_c,1}$ of the critical eigenvalue at the double Hopf aspect ratios $a_{DH}$.

There are discontinuities in $P$ vs $a$ plot in Figure 6 of the transition number which are due to the changes in the critical zonal wavenumber $m_c$. These discontinuities take place at double Hopf bifurcation aspect ratios where two consecutive zonal wavenumbers become critical simultaneously which is investigated in the next section. However, there are also discontinuities in Figure 6, $k = 1$ case (for example near $a = 16$) whose origin is mysterious.

As detailed in Appendix B, the transition number $P$ accounts for two types of nonlinear interactions between the eigenmodes, and is written

$$P = P_0 + P_2,$$

where $P_0$ accounts for nonlinear interactions between the critical modes and the zonally homogeneous modes $m = 0$ (see (B.9) below), while $P_2$ accounts for the interactions between the critical modes and the modes having wavenumbers twice that of the critical modes (see (B.10) below). A comparison of typical numerical values of $P_0$ and $P_2$ shows that $P_2$ is several orders of magnitudes smaller than $P_0$; see Figure 8. We refer to [3, Theorem III.1] for a transition number diagnosing also the type of Hopf bifurcations arising, generically, in delay differential equations, and whose nature is also characterized by the interactions of linearized modes through the model's non-linear terms.

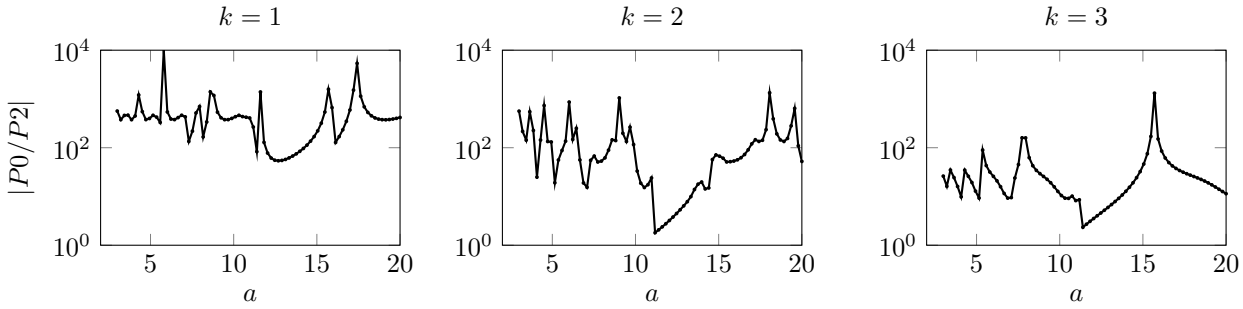


FIGURE 8. The effect of $P_0$ (of $m = 0$ modes) compared to the effect $P_2$ (of $2m_c$ modes) on the transition number.

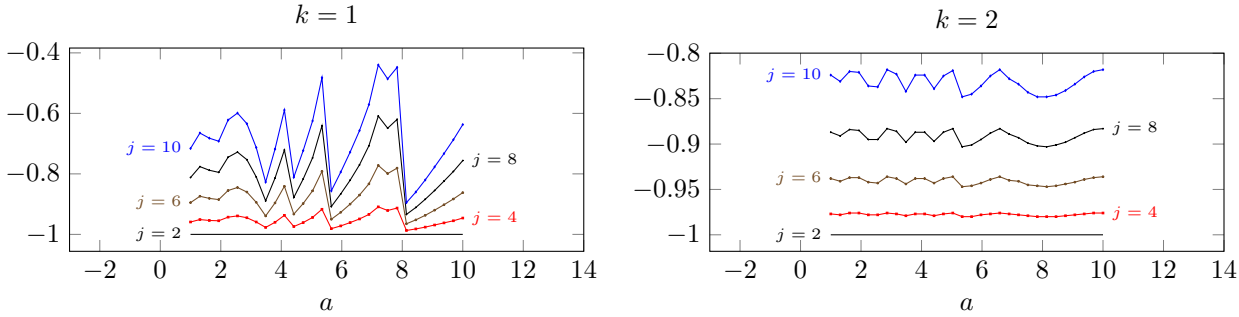


FIGURE 9. $P_{0,j}/|P_{0,2}|$ for even values of $j$. $P_{0,j} = 0$ for odd values of $j$.

Moreover

$$P_0 = \sum_{j=0}^{\infty} P_{0,j}$$

where $P_{0,j}$ measures the contribution of the $j$-th mode with zero wavenumber. Figure 9 shows that the decay of $P_{0,j}$ as $j \to \infty$ is essentially linear. We believe the results in Figure 8 and Figure 9 may help when choosing the modes to include in a simulation when the maximal shear velocity is well above the criticality.

We also compare the dimensional time period of the bifurcated solution (3.8) to the (dimensional) length of the channel in Figure 3.2. With the default parameters as chosen in Table 1, our simulations yield a solution with time period of 180-380 days depending on the channel length of 100-700kms.

3.3. **Double Hopf Bifurcation.** In this section we are interested in the transitions that take place at the critical aspect ratios $a_{DH}$ where four modes with consecutive wavenumbers $m_c$, $m_c + 1$ become unstable as given by the PES condition (3.6).

We first present the reduced equations in this case (for proofs, see Appendix D).

**Lemma 3.2.** *Assume that the first critical eigenvalues have complex multiplicity 2 so that the assumption (3.6) holds. Then, the transition and stability of the steady state solution (2.3) of the equations (2.5) in the vicinity of the critical Reynolds number $\Psi = \Psi_c$ and for any sufficiently small initial condition are equivalent to the stability of the zero solution of the following equations*

$$\begin{aligned} \frac{dz_1}{dt} &= \sigma_{m_c,1} z_1 + z_1(A|z_1|^2 + B|z_2|^2) + o(|z|)^3), \\ \frac{dz_2}{dt} &= \sigma_{m_c+1,1} z_2 + z_2(C|z_1|^2 + D|z_2|^2) + o(|z|)^3), \end{aligned} \tag{3.9}$$

*where $z_1(t), z_2(t) \in \mathbb{C}$ denote the amplitudes of the projection of the solution onto the first eigenfunctions $\psi_{m_c,1}$, $\psi_{m_c+1,1}$ and the **transition numbers** $A, B, C, D$ are determined by the nonlinear interactions of the*

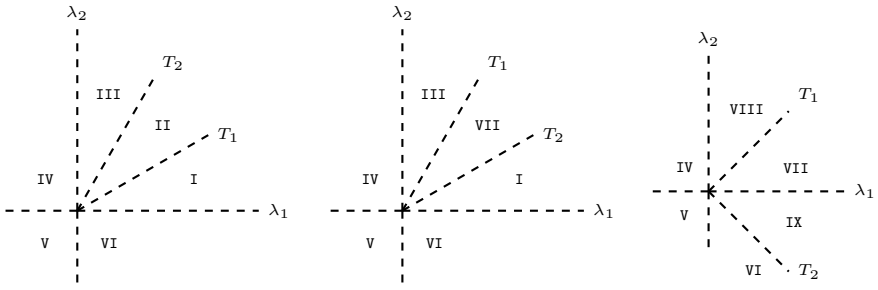


(a) $\theta > 0$, $\delta > 0$, $\theta\delta > 1$ (b) $\theta > 0$, $\delta > 0$, $\theta\delta < 1$ (c) $\theta > 0$, $\delta < 0$

FIGURE 10. The regions in the $\lambda_1$–$\lambda_2$ plane with different dynamical behaviors. In region V, the basic steady state is locally asymptotically stable. In regions IV and VI, the system undergoes a supercritical Hopf bifurcation. The dynamics in regions I, II and III is the double Hopf bifurcation scenario and the details are given in Figure 11. The lines $T_1$ and $T_2$ in the Figure have slopes $1/\theta$ and $\delta$ (as defined in (3.12)) respectively.

*first eigenfunction with higher modes given by (D.2). More precisely, the terms A and D account for the self-interactions among the critical modes, while the terms B and C account for the cross-interactions between the critical modes with the higher modes.*

It is known that the equation (3.9) exhibit a zoo of dynamical behaviors. We refer to [11] for a detailed analysis of all possible cases. Here, we restrict our attention to the case

$$\mathrm{Re}(A) < 0,\ \mathrm{Re}(B) < 0, \mathrm{Re}(B) + \mathrm{Re}(C) < 0, \mathrm{Re}(D) < 0, \tag{3.10}$$

which is the only case we observe in our numerical experiments, see Table 2. Under these conditions it is known that the transition is continuous (see Theorem 2.3 in [12]). For the next theorem, let us define the numbers

$$\lambda_1 = Re(\sigma_{m_c,1}), \qquad \lambda_2 = Re(\sigma_{m_c+1,1}). \tag{3.11}$$

$$\delta = \frac{Re(C)}{Re(A)}, \qquad \theta = \frac{Re(B)}{Re(D)} \tag{3.12}$$

$$\eta_1 = \left(\frac{\lambda_1 - \theta\lambda_2)}{(\theta\delta - 1)\,\mathrm{Re}(A)}\right)^{\frac{1}{2}}, \qquad \eta_2 = \left(\frac{\lambda_2 - \delta\lambda_1}{(\theta\delta - 1)\,\mathrm{Re}(D)}\right)^{\frac{1}{2}}.$$

Recalling $f_{m_c}$ defined in (3.3) (with $m = m_c$), we define the following spatio-temporal profiles

$$\begin{aligned}
\psi_p^{m_c}(x,y,t) &= \left(-\frac{\lambda_1}{\mathrm{Re}(A)}\right)^{\frac{1}{2}} f_{m_c}(x,y,t) + o\left(|\Psi - \Psi_c|^{\frac{1}{2}}\right),\\
\psi_p^{m_c+1}(x,y,t) &= \left(\frac{\lambda_2}{\mathrm{Re}(D)}\right)^{\frac{1}{2}} f_{m_c+1}(x,y,t) + o\left(|\Psi - \Psi_c|^{\frac{1}{2}}\right),\\
\psi_{qp}(x,y,t) &= \eta_1 f_{m_c}(x,y,t) + \eta_2 f_{m_c+1}(x,y,t) + o\left(|\Psi - \Psi_c|^{\frac{1}{2}}\right)
\end{aligned} \tag{3.13}$$

**Theorem 3.2.** *Assume that the conditions of Lemma 3.2 as well as the condition (3.10) hold. Then the equations (2.5) undergo a continuous transition at $\Psi = \Psi_c$, and an $S^3$ attractor $\Sigma$ bifurcates on $\Psi > \Psi_c$, which converges to $\mathbf{0}$ as $\Psi \downarrow \Psi_c$. Depending on the values of $\theta$ and $\delta$, there are three transition scenarios as shown in Figure 10. In each scenario, near the onset of transition $(\lambda_1, \lambda_2) = (0,0)$, $\lambda_1 - \lambda_2$ plane is dissected into several regions with distinct topological structures for the attractor $\Sigma$ as given in Figure 11.*

**Remark 3.1.** *(1) If $z_2 = 0$ or $z_1 = 0$, the equations (3.9) reduce to the equation (3.7) with $A = P$ or $D = P$ respectively. Thus Lemma 3.1 and Theorem 3.1 are special cases of Lemma 3.2 and Theorem 3.2 respectively.*

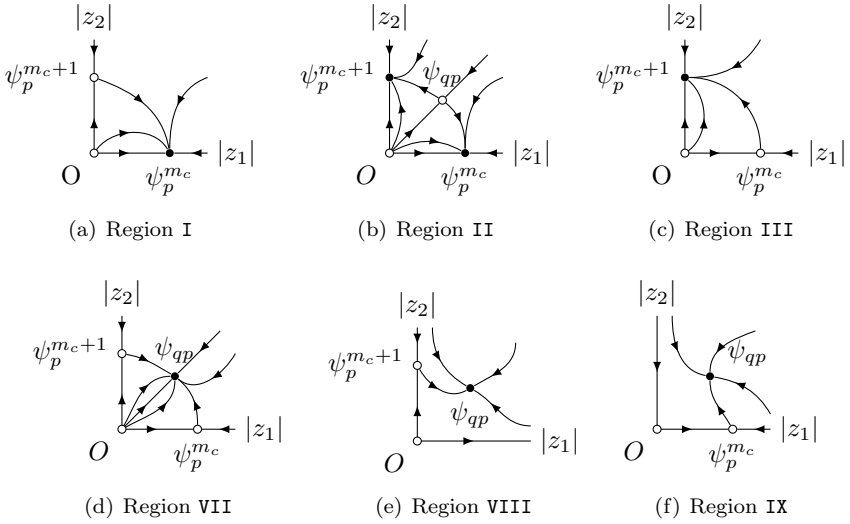


(a) Region I (b) Region II (c) Region III

(d) Region VII (e) Region VIII (f) Region IX

FIGURE 11. The dynamics in the regions given in the first quadrant of Figure 10. $\psi_p^{m_c}$, $\psi_p^{m_c+1}$ are time-periodic with zonal wavenumbers $m_c$ and $m_c+1$ respectively. $\psi_{qp}$ is the quasiperiodic solution given in (3.13).

*(2) We note that the features of the spatial structures of upper vs lower layer of the bifurcated periodic solutions in Figure 2 and the quasi-periodic solution in Figure 12 do not alter much. We expect that the situation would be different if bottom topography is included.*

The transition scenario of double Hopf transition is given by Theorem 3.2 by Figure 10 and Figure 11. We find that near the onset of transition, depending on the fluctuations the basic state transitions either to a time periodic solution or a quasi periodic solution. Our results in Table 2 show that all three of the scenarios presented in Figure 10 are realizable.

In particular, near a double Hopf transition point, one of the following three possibilities must occur post transition, $\Psi > \Psi_c$:

- there is only a single stable limit cycle,
- there are two distinct stable limit cycles, and an unstable quasi-periodic solution
- there is a stable quasi-periodic solution and either one or two unstable limit cycles.

For the double Hopf transition, Theorem 3.2 basically tells that all of the above local structures, the time periodic solution and the 2D torus, if they exist, reside in a local attractor homeomorphic to the three dimensional sphere. The existence of this attracting 3D sphere is guaranteed by the attractor bifurcation theorem, Theorem 6.1 in [15].

## 4. Summary and Discussion

In this paper, we investigated the stability of a parallel zonal jet forced by a Kolmogorov-type wind stress in a periodic zonal channel, using a two-layer quasi-geostrophic (QG) model. This problem is, in terms of complexity, situated between the horizontally unbounded problem [20, 27] and the fully bounded gyre problem [6]. More precisely, the effect of boundaries is captured by the interactions of only a few modes (solutions of the linear stability problem), while still keeping a parallel flow which is connected to the wind-stress field.

Our numerical results show that, as expected based on earlier one ([10, 2, 8, 14]), the zonal shear flow is linearly stable if its maximal amplitude $\Psi$ (or equivalently the maximal amplitude $\tau$ of the wind-stress curl) is below a critical threshold $\Psi_c$. Moreover, as this critical threshold is exceeded, generically a Hopf bifurcation occurs. We approach the problem using dynamic transition theory determining all the attractors near a transition. Under characteristic values of parameters which describe the midlatitude ocean we find that a continuous transition in

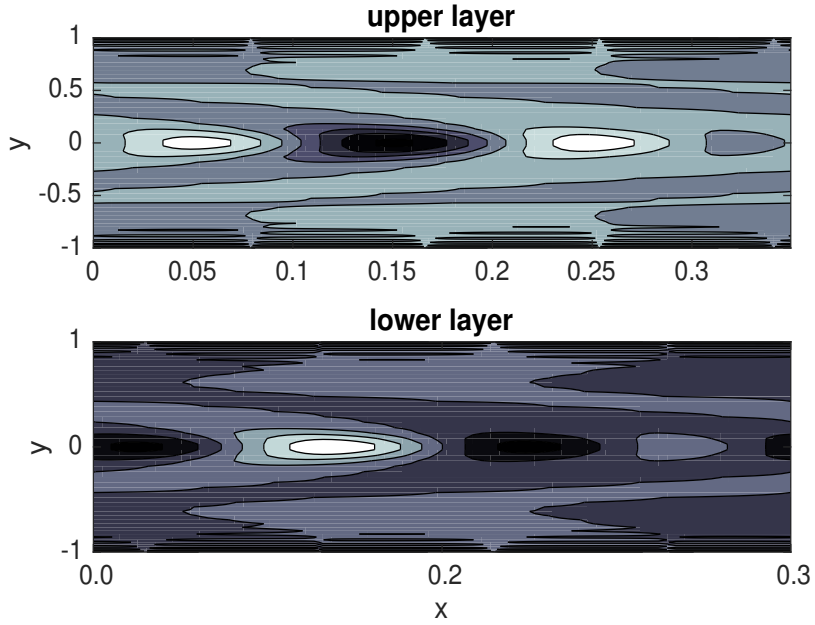


FIGURE 12. Real part of the upper and lower layers of the time quasi-periodic solution $\psi_{qp}$ given in Theorem 3.2 at $t = 0$ for $k = 1$ and $a = 5.722$ where the first two critical wavenumbers are $m_c = 1$ and $m_c = 2$.

the form of supercritical Hopf bifurcation occurs. The numerical results also show that instead of infinitely many modes which effect the type of transition (supercritical vs subcritical Hopf), the transition is indeed determined by the interaction of the first two critical modes with only the first few zonally homogeneous ($m = 0$) modes.

We also investigated the double Hopf bifurcation scenario which takes place at critical length scales where four modes with consecutive wavenumbers become critical. By a rigorous center manifold analysis, we obtain the coefficients of the 4D-ODE system. Our results show that for the parameters we have considered, there exists a quasi-periodic solution which is a linear combination of two periodic solutions and may be stable depending on the parameters. From a transition point of view, in the double Hopf transition, an attractor homeomorphic to 3D sphere bifurcates. This attractor contains stable/unstable limit cycles and an stable/unstable invariant torus (a quasi-periodic solution).

The results add more detail to the nonlinear development of baroclinic instabilities on a non-constant parallel zonal jet, in that the periodic orbits can become unstable to torus bifurcations and give rise to quasi-periodic behavior. Such a scenario was also found for the barotropic double gyre flow [28], but only in a weakly nonlinear framework using a set of (reduced) amplitude equations. The transition scenario found for the zonally periodic zonal jet is likely to be more relevant for the ocean circulation than the sideband instabilities in the zonally unbounded zonal jet case which require a nearby band of wavenumbers to be unstable.

In our set-up, the linear friction coefficient in the upper layer is relatively large and as explained needed to balance the vorticity input by the wind stress for generating the zonal jet. When this friction is decreased, more modes will become unstable near the critical point and their interaction will allow to give a detailed view on the eddy formation process due to baroclinic instabilities. In this way, the dynamic transition theory approach, possibly with extensions as in [4], provides a way forward to develop a mathematical theory of such ocean-eddy formation processes.

**Acknowledgments:** This work has been partially supported by the European Research Council (ERC) under the European Union's Horizon 2020 research and innovation program (grant agreement No. 810370). This study was also supported by a Ben May Center grant.

## Appendix A. Numerical treatment of the linear stability problem

To solve the eigenvalue problem numerically, we first plugin the ansatz

$$\psi(x,y) = e^{i\alpha_m x} Y_j(y), \qquad j \in \mathbb{N}, m \in \mathbb{Z}, \quad \alpha_m := am\pi. \tag{A.1}$$

into the eigenvalue problem

$$\sigma \mathcal{M}\psi(x,y) = \mathcal{N}(y)\psi(x,y),$$

to obtain

$$\sigma \widetilde{\mathcal{M}} Y(y) = \widetilde{\mathcal{N}}(y) Y(y), \qquad Y(y) = (Y_1(y), Y_2(y)) \tag{A.2}$$

Here the linear operators $\widetilde{\mathcal{M}}$ and $\widetilde{\mathcal{N}}(y)$ are defined as

$$\widetilde{\mathcal{M}} = \begin{bmatrix} \Delta_m - F_1 & F_1 \\ F_2 & \Delta_m - F_2 \end{bmatrix}, \qquad \widetilde{\mathcal{N}}(y) = \begin{bmatrix} N_{11} & N_{12} \\ N_{21} & N_{22} \end{bmatrix} \tag{A.3}$$

where

$$\begin{aligned} N_{11} &= c_1 \cos k\pi y \left((k\pi)^2 + \Delta_m\right) - \beta i \alpha_m - r_1 \Delta_m \\ N_{12} &= c_1 F_1 \cos k\pi y \\ N_{21} &= 0 \\ N_{22} &= -c_1 F_2 \cos k\pi y - \beta i \alpha_m - r_2 \Delta_m \end{aligned} \tag{A.4}$$

$$\Delta_m = D^2 - \alpha_m^2, \qquad D = \frac{\partial}{\partial y}$$

$$c_1 = \Psi k\pi i \alpha_m.$$

The eigenvalue problem (A.2) is supplemented with the following boundary conditions

$$Y_i(\pm 1) = D^2 Y_i(\pm 1) = 0, \qquad i = 1, 2. \tag{A.5}$$

We use Legendre-Galerkin method to discretize and solve the (A.2) with boundary conditions (A.5). We refer to [23] for the details of the Legendre-Galerkin method and to [8] for its use in dynamical transition problems. Let $\{L_j\}$ be the Legendre polynomials and consider compact combinations of the Legendre polynomials

$$f_j(y) = L_j(y) + \sum_{k=1}^{4} c_{jk} L_{j+k}(y)$$

with $c_{jk}$ chosen so that $f_j$ satisfy the boundary conditions (A.5), i.e.

$$f_j(\pm 1) = D^2 f_j(\pm 1) = 0.$$

To discretize the eigenvalue problem, we plug

$$Y_i^{N_y}(y) = \sum_{j=0}^{N_y - 1} y_j^{(i)} f_j(y), \qquad \widehat{Y}_i = [y_0^{(i)}, \ldots, y_{N_y-1}^{(i)}]^T, \qquad i = 1, 2. \tag{A.6}$$

into (A.2) to obtain

$$\sigma \begin{bmatrix} \widehat{\Delta}_m - F_1 A_3 & F_1 A_3 \\ F_2 A_3 & \widehat{\Delta}_m - F_2 A_3 \end{bmatrix} \begin{bmatrix} \widehat{Y}_1 \\ \widehat{Y}_2 \end{bmatrix} = \begin{bmatrix} \widehat{N}_{11} & \widehat{N}_{12} \\ \widehat{N}_{21} & \widehat{N}_{22} \end{bmatrix} \begin{bmatrix} \widehat{Y}_1 \\ \widehat{Y}_2 \end{bmatrix} \tag{A.7}$$

$$\begin{aligned} \widehat{N}_{11} &= c_1 (k\pi)^2 A_5 + c_1 \left(A_4^T - \alpha_m^2 A_5\right) - \beta i \alpha_m A_3 - r_1 \widehat{\Delta}_m \\ \widehat{N}_{12} &= c_1 F_1 A_5 \\ \widehat{N}_{21} &= 0 \\ \widehat{N}_{22} &= -c_1 F_2 A_5 - \beta i \alpha_m A_3 - r_2 \widehat{\Delta}_m \end{aligned} \tag{A.8}$$

Here

$$
\begin{aligned}
&A_1 = (D^4 f_j, f_k), \qquad A_2 = (D^2 f_j, f_k), \qquad A_3 = (f_j, f_k),\\
&A_4 = (\cos k\pi y D^2 f_j, f_k), \qquad A_5 = (\cos k\pi y f_j, f_k),\\
&\widehat{\Delta}_m = A_2 - \alpha_m^2 A_3,
\end{aligned} \tag{A.9}
$$

with $(f,g) = \int_{-1}^{1} f(y)g(y)\,\mathrm{d}y$. The explicit expression of the matrices $A_i$, $i = 1,\dots,5$ can be found in [8].

## Appendix B. Proof of Lemma 3.1 and Theorem 3.1

We first proceed with the proof of Lemma 3.1 For this, we denote the adjoint modes by

$$\psi^*_{m,j} = e^{i\alpha_m x} Y^*_m(y).$$

We denote the critical eigenmode and the critical eigenvalue by

$$\psi_c = \psi_{m_c,1}, \qquad \sigma_c = \sigma_{m_c,1}.$$

We denote the bilinear operator $\mathcal{G}$ as

$$\mathcal{G}(u) = G_2(u,u)$$

where $G_2(u,v)$ is linear in each component. Let us define now

$$G_s(u,v) = G_2(u,v) + G_2(v,u). \tag{B.1}$$

The center part of the solution is

$$u_c = z(t)\psi_c + c.c. \tag{B.2}$$

where c.c. stands for complex conjugate of the terms before.

The evolution of $z(t)$ near the onset of transition is obtained by the projection onto the critical mode $\psi_c$.

$$\dot{z} = \sigma_c z + \frac{1}{\langle \mathcal{M}\psi_c, \psi_c^*\rangle}\langle \mathcal{G}(u_c + \Phi), \psi_c^*\rangle. \tag{B.3}$$

where $\Phi$ is the center manifold function. We will obtain its quadratic approximation $\Phi_2$ given by

$$\Phi = \Phi_2(z,\overline{z}) + o(2)$$

Here

$$o(n) = o\left(|(z,\overline{z})|^n\right)$$

denotes higher than $n$-th order terms in $z$, $\overline{z}$.

Using the notation (B.1), the reduced equation (B.3) can be written

$$\dot{z} = \sigma_c z + \frac{1}{\langle \mathcal{M}\psi_c, \psi_c^*\rangle}\langle G_s(u_c, \Phi_2), \psi_c^*\rangle + o(3). \tag{B.4}$$

To obtain a closed system, we need to approximate the center manifold function. The approximation of the center manifold in this case reads, see [22],

$$\Phi_2 = (2\sigma_c - \mathcal{L})^{-1}\Pi_s G_2(z\psi_c, z\psi_c) + (\sigma_c + \overline{\sigma}_c - \mathcal{L})^{-1}\Pi_s G_2(z\psi_c, \overline{z\psi_c}) + c.c. \tag{B.5}$$

where $\mathcal{L} = \Pi_s \mathcal{M}^{-1}\mathcal{N}$ and $\Pi_s$ is the projection on the stable space. Using the formula (B.5), we obtain the expansion of the center manifold as

$$\Phi_2 = z^2 \sum_{j\geq 1} g_{2m_c,j}\psi_{2m_c,j} + |z|^2 \sum_{j\geq 1} g_{0,j}\psi_{0,j} + c.c. \tag{B.6}$$

Here

$$
\begin{aligned}
g_{0,j} &= \frac{1}{(\sigma_c + \overline{\sigma}_c - \sigma_{0,j})\langle \mathcal{M}\psi_{0,j}, \psi^*_{0,j}\rangle}\langle G_2(\psi_c, \overline{\psi_c}), \psi^*_{0,j}\rangle\\
g_{2m_c,j} &= \frac{1}{(2\sigma_c - \sigma_{2m_c,j})\langle \mathcal{M}\psi_{2m_c,j}, \psi^*_{2m_c,j}\rangle}\langle G_2(\psi_c, \psi_c), \psi^*_{2m_c,j}\rangle,
\end{aligned} \tag{B.7}
$$

are the coefficients of the center manifold function.

We write (B.4) as (3.7), that is

$$\dot{z} = \sigma_c z + Pz|z|^2 + o(3).$$

which finishes the proof of Lemma 3.1.

Recalling the definition of $G_s$ given in (B.1), the transition number $P$ can then be written as

$$P = P_0 + P_2, \tag{B.8}$$

where

$$P_0 = \sum_{j\geq 1} P_{0,j}, \qquad P_{0,j} = \frac{1}{\langle \mathcal{M}\psi_c, \psi_c^*\rangle}(g_{0,j} + c.c.)\langle G_s(\psi_c, \psi_{0,j}), \psi_c^*\rangle, \tag{B.9}$$

denotes the contribution of $m = 0$ modes $\psi_{0,j}$ while

$$P_2 = \sum_{j\geq 1} P_{2,j}, \qquad P_{2,j} = \frac{1}{\langle \mathcal{M}\psi_c, \psi_c^*\rangle} g_{2m_c,j}\langle G_s(\overline{\psi_c}, \psi_{2m_c,j}), \psi_c^*\rangle, \tag{B.10}$$

denotes the contribution of $2m_c$ modes $\psi_{2m_c,j}$ on the transition number respectively. The transition depends on the real part of the transition number $P$. The proof of Theorem 3.1 follows from the standard Hopf bifurcation analysis of the reduced equation.

## Appendix C. Practical aspects for the calculation of the transition number

The practical calculation of the $P_0$-term in (B.9) and the $P_2$-term in (B.10), boils down to the efficient calculation of the inner and trilinear products involved therein. In that respect, we provide here explicit expressions of the latter. They are given by

$$\begin{aligned}\langle \mathcal{M}\psi_{m,j}, \psi_{m,j}^*\rangle = i\alpha_m \int_{-1}^{1} \left((D^2 - \alpha_m^2 - F_1)Y_{m,j}^1 + F_1 DY_{m,j}^2\right)\overline{Y_{m,j}^{*1}}\,\mathrm{d}y \\ + i\alpha_m \int_{-1}^{1} \left((D^2 - \alpha_m^2 - F_2)Y_{m,j}^2 + F_2 DY_{m,j}^1\right)\overline{Y_{m,j}^{*2}}\,\mathrm{d}y,\end{aligned}$$

and

$$\begin{aligned}\langle G_2(\psi_{m,j}, \psi_{n,k}), \psi_{p,l}^*\rangle &= -\delta_{m+n-p}\left(\int_{-1}^{1} G_2^1\overline{Y_{p,l}^{*,1}} + G_2^2\overline{Y_{p,l}^{*,2}}\right)\mathrm{d}y,\\ G_2^1 &= i\alpha_m Y_{m,j}^1\left(D(D^2 - \alpha_n^2 - F_1)Y_{n,k}^1 + F_1 DY_{n,k}^2\right)\\ &\quad - i\alpha_n\left((D^2 - \alpha_n^2 - F_1)Y_{n,k}^1 + F_1 Y_{n,k}^2\right)DY_{m,j}^1\\ G_2^2 &= i\alpha_m Y_{m,j}^2\left(D(D^2 - \alpha_n^2 - F_2)Y_{n,k}^2 + F_2 DY_{n,k}^1\right)\\ &\quad - i\alpha_n\left((D^2 - \alpha_n^2 - F_2)Y_{n,k}^2 + F_2 Y_{n,k}^1\right)DY_{m,j}^2.\end{aligned}$$

In practice, the integrals can be evaluated by any commonly used quadrature rules in which the values of the integrand are evaluated at quadrature points. In our calculations, we use

$$\int_{-1}^{1} f(y)\,\mathrm{d}y = \sum_{n=0}^{N_y} f(y_n)\omega_n,$$

where $y_n$ and $\omega_n$ are Legendre-Gauss-Lobatto quadrature points and weights respectively.

## Appendix D. Proof of Lemma 3.2 and Theorem 3.2

As the reduction in the case of (3.6) is similar to the case of (3.5) given in the previous section, we will only mention the differences between these two cases. Under the assumption (3.6), we write the center part of the solution as

$$u_c = z_1(t)\psi_1 + z_2(t)\psi_2 + c.c.$$

where the first two critical modes are

$$\psi_1 = \psi_{m_c,1}, \quad \psi_2 = \psi_{m_c+1,1}, \quad \psi_{-1} = \psi_{-m_c,1}, \quad \psi_{-2} = \psi_{-m_c-1,1}.$$

with corresponding eigenvalues

$$\sigma_1 = \sigma_{m_c,1}, \quad \sigma_2 = \sigma_{m_c+1,1}, \quad \sigma_{-1} = \sigma_{-m_c,1}, \quad \sigma_{-2} = \sigma_{-m_c-1,1}$$

The equation (B.4) becomes the system

$$\dot{z}_j = \sigma_j z_j + \frac{1}{\langle \mathcal{M}\psi_j, \psi_j^* \rangle} \langle \mathcal{G}(u_c + \Phi_2), \psi_j^* \rangle + o(3), \qquad j = 1, 2. \tag{D.1}$$

and the center manifold function (B.5) is replaced by

$$\Phi_2 = \sum_{|j|,|k|=1}^{2} z_j z_k \Psi_{j,k} + o(2), \qquad \Psi_{j,k} = (\sigma_j + \sigma_k - \mathcal{L})^{-1} \Pi_s G_2(\psi_j, \psi_k).$$

Now, the equations (D.1) become (3.9) with the coefficients defined as below.

$$\begin{aligned}
A &= g_{1,1,-1,1} + g_{1,-1,1,1} + g_{-1,1,1,1} \\
B &= g_{1,2,-2,1} + g_{1,-2,2,1} + g_{2,1,-2,1} + g_{2,-2,1,1} + g_{-2,1,2,1} + g_{-2,2,1,1} \\
C &= g_{2,1,-1,2} + g_{2,-1,1,2} + g_{1,2,-1,2} + g_{1,-1,2,2} + g_{-1,2,1,2} + g_{-1,1,2,2} \\
D &= g_{2,2,-2,2} + g_{2,-2,2,2} + g_{-2,2,2,2} \\
g_{i,j,k,l} &= \frac{1}{\langle \mathcal{M}\psi_l, \psi_l^* \rangle} \langle G_s(\psi_i, \Psi_{j,k}, \psi_l^*) \rangle, \\
\Psi_{j,k} &= (\sigma_j + \sigma_k - \mathcal{L})^{-1} \Pi_s G_2(\psi_j, \psi_k)
\end{aligned} \tag{D.2}$$

We note that the above coefficients contain only $g_{i,j,k,l}$ for which $i + j + k = l$. The expansion of the center manifold coefficients can be written more explicitly as

$$\Psi_{j,k} = \sum_{i=1}^{\infty} \frac{\langle G_2(\psi_{m_j}, \psi_{m_k}), \psi_{m_j+m_k,i}^* \rangle}{\langle \mathcal{M}\psi_{m_j+m_k,i}, \psi_{m_j+m_k,i}^* \rangle} (\sigma_j + \sigma_k - \sigma_{m_j+m_k})^{-1} \psi_{m_j+m_k,i}$$

Now we analyze the equations (3.9) by first putting them in polar form

$$z_j = \rho_i e^{i\gamma_j}, \quad j = 1, 2$$

which yields

$$\begin{aligned}
\dot{\rho_1} &= Re(\sigma_1)\rho_1 + \rho_1(Re(A)\rho_1^2 + Re(B)\rho_2^2) + \text{ h.o.t.} \\
\dot{\rho_2} &= Re(\sigma_2)\rho_2 + \rho_2(Re(C)\rho_1^2 + Re(D)\rho_2^2) + \text{ h.o.t.}
\end{aligned} \tag{D.3}$$

and

$$\begin{aligned}
\dot{\gamma_1} &= Im(\sigma_1) + \text{ h.o.t.} \\
\dot{\gamma_2} &= Im(\sigma_2) + \text{ h.o.t.}
\end{aligned}$$

For the specific case of (3.10), the equations (D.3) always admit the solutions which represent the periodic solutions

$$\begin{aligned}
(\rho_1, \rho_2) &= \left( -\frac{Re(\sigma_1)}{Re(A)}, 0 \right), \\
(\rho_1, \rho_2) &= \left( 0, -\frac{Re(\sigma_2)}{Re(D)} \right),
\end{aligned}$$

with respective eigenvalues

$$\begin{aligned}
\kappa_1 &= -2\sigma_1, \qquad \kappa_2 = \sigma_2 - \delta\sigma_1 \\
\kappa_1 &= -2\sigma_2, \qquad \kappa_2 = \sigma_1 - \theta\sigma_2
\end{aligned}$$

Also, the equations (D.3) admit the following solution which represents a quasi-periodic solution

$$(\rho_1, \rho_2) = \left( \frac{\sigma_1 - \theta\sigma_2}{Re(A)(\theta\delta - 1)}, \frac{\sigma_2 - \delta\sigma_1}{Re(D)(\theta\delta - 1)} \right).$$

Since the Jacobian matrix of the right hand side of (D.3) at the quasi-periodic solution has determinant

$$\frac{-4(\sigma_2-\delta\sigma_1)(\sigma_1-\theta\sigma_2)}{\theta\delta-1}.$$

With this information, the transition scenarios summarized in Figure 10 and Figure 11 can be obtained by a standard analysis. To prove the claim on the bifurcation of an $S^3$-attractor, we need to prove that $(\rho_1,\rho_2)=(0,0)$ is locally stable equilibrium of (D.3) at $\Psi=\Psi_c$, that is when $\mathrm{Re}(\sigma_1)=\mathrm{Re}(\sigma_2)=0$. In this case by assumption (3.10), from (D.3), we can obtain

$$\frac{d}{dt}(\rho_1^2+\rho_2^2)=Re(A)\rho_1^4+(\mathrm{Re}(B)+\mathrm{Re}(C))\rho_1^2\rho_2^2+\mathrm{Re}(D)\rho_2^4<0$$

which proves the claim.

| | | |
|---|---|---|
| $L_y$ | meridional length scale | $10^6$ m |
| $H_1$ | upper layer depth | 250m |
| $H_2$ | upper layer depth | 750m |
| $\Delta\rho$ | density difference | $\rho_2-\rho_1=1$ kgm$^{-3}$ |
| $U$ | characteristic velocity | $\tau_0/(\rho_0 H_1\beta_0 L_y)=0.02$ m s$^{-1}$ |
| $\tau_0$ | characteristic zonal wind stress | 0.1 Pa |
| $\beta_0$ | planetary vorticity gradient | $2\times10^{-11}$ (ms)$^{-1}$ |
| $f_0$ | reference Coriolis parameter | $10^{-4}$ s$^{-1}$ |
| $\epsilon_0$ | bottom friction coefficient | $10^{-7}$ s$^{-1}$ |
| $g$ | gravitational acceleration | 9.8 ms$^{-2}$ |
| $g'$ | reduced gravity | $g\Delta\rho/\rho_0=0.01$ ms$^{-2}$ |
| $\rho_0$ | reference density | $10^3$ kgm$^{-3}$ |
| $F_1$ | upper layer Froude number | $f_0^2L_y^2/(g'H_1)=4000$ |
| $F_2$ | lower layer Froude number | $f_0^2L_y^2/(g'H_2)=4000/3$ |
| $\beta$ | planetary vorticity factor | $\beta_0L_y^2/U=1000$ |
| $\tau$ | wind-stress parameter | 1.0 |
| $r_2$ | lower layer linear friction coefficient | $r_2=\epsilon_0L_y/U=5.0$ |

TABLE 1. Model parameters.

## REFERENCES


[1] H. Brézis. *Functional Analysis, Sobolev Spaces and Partial Differential Equations*. Springer, 2010.

[2] Ming Cai, Marco Hernandez, KiahWah Ong, and Shouhong Wang. Baroclinic Instability and Transitions in a Two-Layer Quasigeostrophic Channel Model. *arXiv:1705.07989 [physics]*, April 2017.

[3] M. D. Chekroun, I. Koren, and H. Liu. Efficient reduction for diagnosing hopf bifurcation in delay differential systems: Applications to cloud-rain models. *Chaos*, 30(5):053130, 2020.

[4] Mickaël D Chekroun, Honghu Liu, and James C McWilliams. Variational Approach to Closure of Nonlinear Dynamical Systems: Autonomous Case. *Journal of Statistical Physics*, 179(5):1073–1160, December 2019.

[5] H A Dijkstra. *Nonlinear Physical Oceanography: A Dynamical Systems Approach to the Large Scale Ocean Circulation and El Niño, 2nd Revised and Enlarged edition*. Springer, New York, 532 pp., 2005.

[6] H A Dijkstra and C. A. Katsman. Temporal variability of the Wind-Driven Quasi-geostrophic Double Gyre Ocean Circulation: Basic Bifurcation Diagrams. *Geophys. Astrophys. Fluid Dyn.*, 85:195–232, 1997.

| $k$ | $m_c$ | $a_{DH}$ | $\Psi_c$ | $Re(A)$ | $Re(B)$ | $Re(C)$ | $Re(D)$ | $\delta$ | $\theta$ | $\delta\theta$ |
|---|---|---|---|---|---|---|---|---|---|---|
| 1 | 1 | 11.26 | 0.10 | -0.25 | -1.00 | 0.01 | -0.33 | -0.05 | 3.08 | -0.15 |
| 1 | 2 | 7.30 | 0.10 | -0.37 | -1.00 | -0.13 | -0.40 | 0.36 | 2.51 | 0.89 |
| 1 | 3 | 5.38 | 0.10 | -0.95 | -1.00 | -0.22 | -0.61 | 0.23 | 1.65 | 0.37 |
| 1 | 4 | 4.23 | 0.09 | -0.81 | -1.00 | -0.29 | -0.61 | 0.36 | 1.63 | 0.58 |
| 2 | 1 | 11.18 | 0.05 | -0.15 | -1.00 | 0.12 | -0.23 | -0.77 | 4.39 | -3.38 |
| 2 | 2 | 7.20 | 0.05 | -0.34 | -1.00 | -0.04 | -0.46 | 0.13 | 2.20 | 0.28 |
| 2 | 3 | 5.27 | 0.05 | -0.37 | -1.00 | -0.14 | -0.45 | 0.38 | 2.24 | 0.86 |
| 2 | 4 | 4.14 | 0.05 | -0.38 | -1.00 | -0.21 | -0.44 | 0.55 | 2.25 | 1.25 |

TABLE 2. The double Hopf transition numbers. Here $k = 1, 2$ is the wavenumber of the forcing, $m_c$ and $m_c + 1$ are the wavenumbers of the first two critical modes which become unstable simultaneously at the critical aspect ratio $a_{DH}$. $A$, $B$, $C$, $D$ are the coefficients of the double Hopf transition normalized with respect to the maximum absolute value of those coefficients. The parameters $\delta$ and $\theta$ are defined by (3.12).


[7] H A Dijkstra and Van der Vaart, P. C. F. On the physics of upgradient momentum transport in unstable eastward jets. *Geophys. Astrophys. Fluid Dyn.*, 88:295–323, 1998.

[8] Henk Dijkstra, Taylan Sengul, Jie Shen, and Shouhong Wang. Dynamic Transitions of Quasi-geostrophic Channel Flow. *SIAM Journal on Applied Mathematics*, 75(5):2361–2378, January 2015.

[9] E. T. Eady. Long waves and cyclone waves. *Tellus*, 1:33–52, 1949.

[10] Chanh Kieu, Taylan Sengul, Quan Wang, and Dongming Yan. On the Hopf (double Hopf) bifurcations and transitions of two-layer western boundary currents. *Communications in Nonlinear Science and Numerical Simulation*, 65:196–215, December 2018.

[11] Yuri Kuznetsov. *Elements of Applied Bifurcation Theory*. Applied Mathematical Sciences. Springer-Verlag, New York, third edition, 2004.

[12] Kevin Li. Dynamic Transitions of the Swift-Hohenberg Equation with Third-Order Dispersion. *arXiv:2007.15722 [math-ph]*, July 2020.

[13] A. F. Lovegrove, I. M. Moroz, and P. L. Read. Bifurcations and instabilities in rotating, two-layer fluids: II. $\beta$-plane. *Nonlinear Processes in Geophysics*, 9(3/4):289–309, August 2002.

[14] ChunHsien Lu, Yiqiu Mao, Taylan Sengul, and Quan Wang. On the spectral instability and bifurcation of the 2D-quasi-geostrophic potential vorticity equation with a generalized Kolmogorov forcing. *Physica D: Nonlinear Phenomena*, 403:132296, February 2020.

[15] Tian Ma and Shouhong Wang. *Bifurcation Theory and Applications*, volume 53 of *World Scientific Series on Nonlinear Science Series A*. World Scientific, June 2005.

[16] Tian Ma and Shouhong Wang. *Phase Transition Dynamics*. Springer International Publishing, Cham, 2019.

[17] L. D. Meshalkin and Ia. G. Sinai. Investigation of the stability of a stationary solution of a system of equations for the plane movement of an incompressible viscous liquid. *Journal of Applied Mathematics and Mechanics*, 25(6):1700–1705, January 1961.

[18] J Pedlosky. *Geophysical Fluid Dynamics. 2nd Edn.* Springer-Verlag, New York, 1987.

[19] Joseph Pedlosky. Finite-Amplitude Baroclinic Waves. *Journal of the Atmospheric Sciences*, 27(1):15–30, January 1970.

[20] N. A. Phillips. A simple three-dimensional model for the study of large-scale extratropical flow patterns. *J. Meteor.*, 8:381–394, 1951.

[21] R. D. Romea. The effects of friction and $\beta$ on finite amplitude baroclinic waves. . *Journal of Atmospheric Science*, 34:1689–1695, 1977.

[22] Taylan Şengül and Shouhong Wang. Dynamic Transitions and Baroclinic Instability for 3D Continuously Stratified Boussinesq Flows. *Journal of Mathematical Fluid Mechanics*, 20(3):1173–1193, September 2018.

[23] Jie Shen, Tao Tang, and Li-Lian Wang. *Spectral Methods*, volume 41 of *Springer Series in Computational Mathematics*. Springer Berlin Heidelberg, Berlin, Heidelberg, 2011.

[24] Eric Simonnet, Michael Ghil, Shouhong Wang, and Zhi-Min Chen. Hopf bifurcation in quasi-geostrophic channel flow. *SIAM Journal on Applied Mathematics*, 64(1):343–368, 2003.

[25] L. Talley. *Descriptive Physical Oceanography*. Academic Presss, New York, 2011.

[26] G. Vallis. *Atmospheric and Oceanic Fluid Dynamics*. Cambridge University Press, Cambridge, UK, 2006.

[27] P. C. F. Van der Vaart and H. A. Dijkstra. Sideband instabilities of mixed barotropic/baroclinic waves growing on a midlatitude zonal jet. *Phys. Fluids*, 9:615–631, 1997.
[28] Van der Vaart, P. C. F., H M Schuttelaars, D Calvete, and H A Dijkstra. Instability of time-dependent wind-driven ocean gyres. *Physics of Fluids*, 14:3601–3615, 2002.
[29] Pierre Welander. A two-layer frictional model of wind-driven motion in a rectangular oceanic basin. *Tellus*, 18(1):54–62, January 1966.

(Chekroun) Department of Earth and Planetary Sciences, Weizmann Institute, Rehovot 76100, Israel
*Email address*: michael-david.chekroun@weizmann.ac.il

(Dijkstra) Centre for Complex System Studies, Department of Physics, Utrecht University, Utrecht, The Netherlands
*Email address*: h.a.dijkstra@uu.nl

(Şengül) Department of Mathematics, Marmara University, 34722 Istanbul, Turkey
*Email address*: taylan.sengul@marmara.edu.tr

(Wang) Department of Mathematics, Indiana University, Bloomington, IN 47405
*Email address*: showang@indiana.edu, http://www.indiana.edu/~fluid